Batteries & Supercaps

Chemistry Europe
European Chemical Societies Publishing
Batteries & Supercaps

RESEARCH ARTICLE OPEN ACCESS

Degradation Pathways of Carbonate-Based Electrolyte Formulations in Potassium Vanadium Phosphate/Graphite Potassium-Ion Batteries

Celine Röder | Ulf-Christian Rauska | Andreas Hofmann | Andreas Heyn | Valeriu Mereacre | Joachim R. Binder | Fabian Jeschull

Karlsruhe Institute of Technology (KIT), Institute for Applied Materials (IAM), Eggenstein-Leopoldshafen, Germany

Correspondence: Fabian Jeschull (fabian.jeschull@kit.edu)

Received: 21 April 2026 | **Revised:** 15 June 2026 | **Accepted:** 22 June 2026

Keywords: electrolyte additives | electrolyte degradation | gas chromatography/mass spectrometry | graphite | potassium-ion battery | potassium vanadium phosphate | X-ray photoelectron spectroscopy

ABSTRACT

Electrolyte development for potassium-ion batteries (KIBs) pose great challenges due to the high intrinsic reactivity of the K-ion system as well as the desired high-voltage application of KIBs, which often trigger strong decomposition of the electrolyte at the electrode interfaces. A common approach to tailor the electrolyte's properties is the use of cosolvents and additives. While their role in lithium- and sodium-based systems is progressively elucidated and even become established as standard cell components, the impact in KIBs still demands for a fundamental investigation. In this study, a comparative analysis of K-ion full cells based on a potassium vanadium phosphate cathode (KVP/C) and a graphite anode employing several electrolyte formulations was carried out to shed light on the complex interrelations of cyclability and the use of prevalent electrolyte additives. Thereby, vinylene carbonate (VC) was determined as most promising additive for next-generation high-voltage KIBs.

1 | Introduction

The development of potassium-ion batteries (KIBs) strongly benefits and builds upon the advances in other monovalent cell chemistries, lithium and sodium. For instance, graphite is a convenient active material for negative electrodes with a low average redox potential (≈0.2 – 0.3 V vs. K^+/K) and a theoretical capacity of 279 mAh g^{-1} [1–5]. Major challenges include poorly stable solid electrolyte interphase (SEI) layers and the mechanochemistry of the potassium intercalation into graphite with a volume expansion of ca. 60% [1, 2, 6], which leads to recurrent electrolyte degradation and SEI reformation at the negative electrode. The choice for suitable positive electrode materials focuses currently on either Prussian blue analogs (PBAs) or polyanionic compounds [7–14]. To date, a large fraction of KIB full-cell development has been centered on PBA/graphite systems, which have emerged as the most widely studied cell configuration in the field [15–17]. Within the pool of different polyanionic materials, vanadium-based polyphosphates have gained growing interest in the community. Previously reported derivatives include $KVPO_4F$ [18], $KVOPO_4$ [15], or $KVPO_4F_{0.5}O_{0.5}$ (KVPFO) [14] that enable average cell voltages around 4.0 V versus K^+/K graphite-based full-cell configurations. Limitations of the material class include, for example, low intrinsic electronic conductivities that have to be addressed by carbon coatings, electrolyte degradation at high positive potentials, and lower theoretical capacities in the range from 55 to 95 mAh g^{-1} compared to Fe/Mn-based PBAs.

$K_3V_2(PO_4)_3$ (KVP) features another promising cathode material which offers a fluorine-free and easy producible active compound [19, 20]. With this background, our group recently presented a scalable synthesis approach to produce microstructured KVP/C composites, as an important step toward more standardized

material, electrode, and cell tests in lab- or pilot-scale environments [21].

Based on a meta study by Hosaka and Komaba in 2022 [22], carbonate-based electrolytes, in particular mixtures of ethylene carbonate (EC) with propylene carbonate (PC), diethyl carbonate (DEC), or dimethyl carbonate (DMC), and KPF_6 as conductive salts are still the most commonly used. In combination with graphite electrodes, these formulations are still among the electrolytes providing the best trade-off in terms of SEI formation (passivation) and electrochemical properties [23–25]. Out of the electrolyte additives that were previously suggested, 1,3,2-dioxathiolane 2,2-dioxide (DTD) [26, 27], fluoroethylene carbonate (FEC) [28, 29], and vinylene carbonate (VC) [30, 31] are the most commonly used additives in combination with carbonate-based electrolytes (list not extensive). Despite their positive impact for both negative and positive electrodes, many of the reported results were obtained from half cell experiments (i.e., against a potassium metal counter electrode), which raises the question, how much of the improvement is actually assigned to more effect passivation of the potassium metal electrode. Hosaka et al. [26] demonstrated, for example, that DTD suppresses the detrimental formation of bis(alkyl carbonates) in EC/(linear carbonate) solvent mixtures in contact with potassium metal. However, in full cell configurations with a graphite negative electrode, DTD can be detrimental to the overall electrochemical process [26, 27]. Based on our own results, the SEI properties are therefore substantially different for samples prepared in half cells as compared to those prepared in full cells [4]. These differences become most apparent when compared to corresponding lithium systems [3]. For this reason, it is paramount to crosscheck promising electrolyte formulations in full cell setups, ideally with standardized materials to act as reference for performance indicators. This approach was outlined previously, for example, by Larhrib et al. for a graphite/KVPFO [32].

Herein, we present a comprehensive study on the impact of carbonate-based electrolyte formulations on the electrochemical characteristics of KVP/graphite K-ion full cells. Our study includes two commonly used carbonate mixtures, EC/PC and EC/DEC, the electrolytes additives FEC and VC. The early stages of SEI formation and aging were investigated by a complementary analytical approach with a strong focus on the graphite electrode as a main source of loss of charge inventory and degradation processes. Our study employed X-ray photoelectron spectroscopy (XPS), surface-sensitive information, (cross section) scanning electron microscopy (SEM), and energy-dispersive X-ray spectroscopy (EDX) for morphological changes and elemental distribution, as well as gas chromatography/mass spectrometry (GC/MS) to quantify soluble electrolyte degradation products. This work illustrates in a comprehensive manner how electrolyte mixtures of EC/PC in combination with the electrolyte additive VC improves the SEI properties and thus reduces irreversible losses in the full cell setup, which enabled balanced full cell configurations that run at a capacity retention of 60% for over 200 cycles. Our results provide key lessons in designing K-ion batteries based on polyanionic positive electrode materials and valuable insights in system parameters that lay a basis for the transfer to larger cell formats.

2 | Results and Discussion

This study is structured in two parts: In the first section, graphite/KVP full cells are introduced as lab-scale benchmark to test different carbonate-based electrolyte formulations. The test matrix comprises two base solvent mixtures, EC/PC and EC/DEC and either FEC or VC as additives, respectively (for structural formulas, see Figure 1). The selection of electrolyte formulations is well motivated by a large fraction of recent works that employ EC-based electrolyte mixtures, as demonstrated, for example, in a meta study performed by Hosaka and Komaba [22]. We stress explicitly that none of the electrodes was preconditioned in any way prior to cell assembly. From a practical point-of-view strategies, such as precycling electrodes to mask initial losses of the charge carrier inventory is not a viable approach and hence avoided herein deliberately. The second section studies SEI formation and electrolyte degradation in the early stages of cycling (first 10 cycles) that determine the cycle life of the cell to a significant degree.

2.1 | Long-Term Cycling of Potassium Vanadium Phosphate/Graphite Potassium-Ion Batteries

The KVP/graphite cells were galvanostatically cycled at current rate of C/20 ($1C_{theoretical} = 106\,mAh\,g^{-1}$) within the voltage limits of 2.0–4.4 V, until their capacity retention dropped below the threshold of <50%. The voltage limits were derived from previous work on related cell system [21, 27]. Multiple cells containing identical electrolyte samples were subjected to repeated cycling to assess reproducibility, as shown in Figure S2. In Figure 2, the cycling results of four formulations are shown, including the two basic electrolyte formulations without additives (further denoted as EC/PC and EC/DEC), as well as formulations comprising EC/PC + 2 vol.% FEC and EC/PC + 1 vol.% VC (further denoted as FEC-2 and VC-1). Additional cycling data of other electrolyte compositions are provided in the Supporting Information (Figure S1). For this study, FEC contents between 0.5 and 2 vol.%, and VC contents between 0.5 – 5.0 vol.% were tested. The additive amounts correspond to established concentration windows used in graphite-based Li-ion batteries [33–35]. In the comparison in Figure 2, the sample with 1 vol.% VC and 2 vol.% FEC was

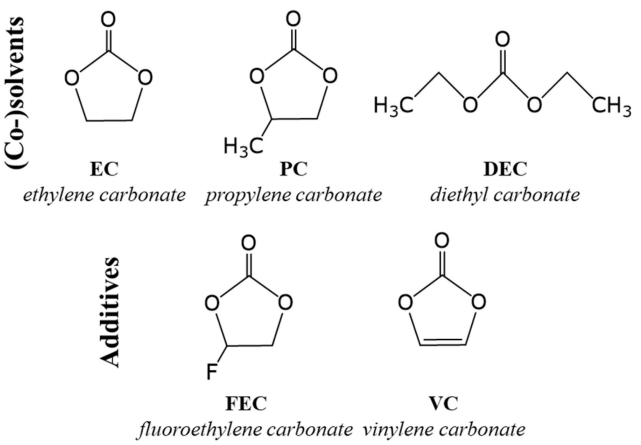

FIGURE 1 | Structural formulas of the organic (co)solvents and additives used in the different electrolyte formulations.

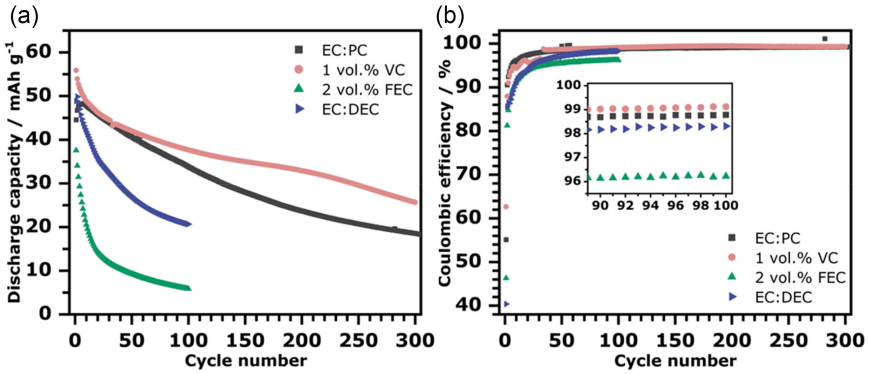

FIGURE 2 | Electrochemical performance of tested cells. (a) Discharge capacities over long cycle of the full cells with different electrolytes. (b) Coulombic efficiency of the same cells. Cells were cycled for a minimum of 100 cycles or until a capacity loss of 50%.

used. The latter induced faster cell deterioration with increasing FEC amount, all of which performed poorer than the FEC-free case (further discussed below). Therefore, for the XPS analysis below, the 2 vol.% FEC electrolyte was expected to show more pronounced interphase-related signatures and distinct degradation products, which motivated its choice in this comparison over formulations with lower additive content. For VC, an optimum appears to be reached at a concentration of around 1 vol.%.

The graphite active material in this work allows the use of EC/PC without any marked exfoliation, which is presumably due to a functional surface coating (the proprietary carbon surface coating according to manufacturer information). The KVP/graphite cells reached first cycle capacities between 50 and 56 mAh g^{-1}. The average discharge voltage was 3.6 ± 0.3 V at a specific capacity of 45 ± 10 mAh g^{-1} after the first two formation cycles. The initial capacities for the four samples herein are thus similar to the values determined in our previous work on KVP/C against metallic potassium [21]. The highest initial CE was observed for the VC-1 formulation with 62.7%. Considering this rather low CE, it is surprising that the cell maintained a capacity retention of more than 60% over more than 200 cycles. This result is an indication that the loss of active charge carrier inventory which is lower than the degree of parasitic reactions derived from the C.E. would suggest (see *Discussion Section*). The 80% capacity retention threshold was reached for both EC/PC and VC-1 electrolyte formulations after around 60 and 80 cycles, respectively. Without VC, the degradation was more substantial, while with VC, a notable knee point in the capacity retention marks the onset of accelerated degradation. A synopsis of the key parameters is shown in Table 1. The cells were assembled with an initial oversized cathode, yielding N/P <1, in order to account for irreversible K-ion losses from SEI formation and parasitic reactions, as indicated by the low Coulombic efficiencies during the first cycles. The cumulative loss of cyclable potassium effectively shifts the electrode balancing toward higher N/P ratios. This evolution is reflected in the voltage profiles and dQ/dV analysis, where a progressive suppression and truncation of high-voltage cathode features is observed. Such behavior is consistent with a transition from initially anode-limited operation to increasingly cathode-limited behavior upon cycling.

2.1.1 | *Voltage Profiles*

The voltage profiles, shown in Figure 3a, are plotted for selected cycles from the 1st up to the 300th cycle for each electrolyte system. The first charge sequence shows that in EC/PC-based electrolytes, specific capacities of between 70 and 85 mAh g^{-1} are reached, whereas in the EC/DEC electrolyte, a considerably longer first charge is observed that is likely related to the side reaction of EC and DEC, and potentially degradation products thereof [27, 36]. Despite the large apparent electrolyte degradation, the first cycle initial discharge capacity is about as high as the best performing EC/PC mixture that contained 1 vol.% VC. The KVP/graphite cell in VC-1 delivered 56 mAh g^{-1}, while in electrolytes without additives, the initial specific capacity on discharge was below 50 mAh g^{-1}. The color gradients clearly demonstrate that the VC-1 sample outperformed other electrolyte composition in terms of capacity retention (Figure 3a). More specifically, VC-1 performed better because the cell showed significantly smaller increase in overpotential and preserved characteristic features in the profile over a considerably longer time (Figures 3 and S3). This becomes

TABLE 1 | Summarized key parameters of the cycling data.

Electrolyte	N/P ratio[a]	Initial discharge capacity, mAh g^{-1}	80% retention reached in cycle[b]	Initial CE, %	CE after 100 cycles, %	Cum. irreversible charge loss after 100 cycles, %
EC/PC	0.89	44.6	66	55.1	98.8	27
VC-1	0.88	55.9	82	62.7	99.1	28
FEC-2	0.90	37.6	15	46.3	96.2	83
EC/DEC	0.91	48.9	27	40.4	98.3	57

[a]Calculated using the areal capacities of the electrodes.
[b]First value taken after 10 cycles preconditioning.

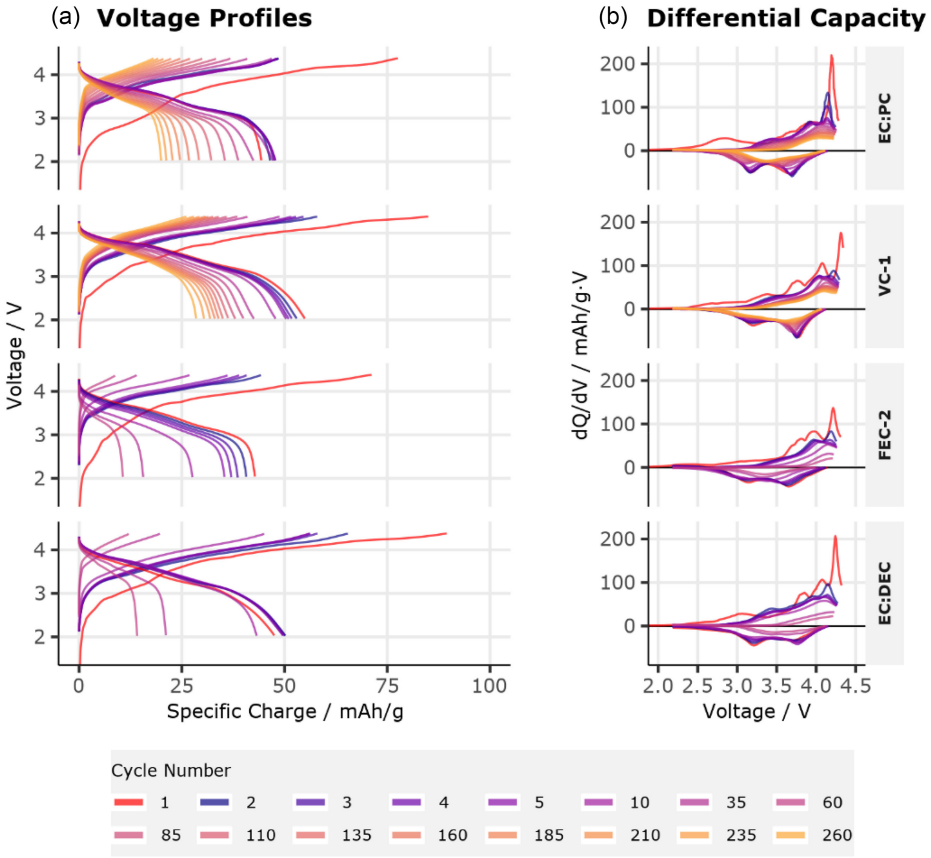

FIGURE 3 | (a) Selected voltage profiles and corresponding (b) differential capacity plots of KVP/graphite full cells cycled in different electrolyte formulations.

most apparent in the comparison with other samples beyond the 20th cycle (see Figure S3). For instance, upon charge, the charge processes show notably higher overpotentials, leading to shorter charging sequences as the upper cutoff limit is reached prematurely. Upon discharge, the upper voltage step from 4.0 to about 3.7 V fades rapidly after the 10th cycle, and the voltage profile straightens out to an almost linear voltage decrease over large parts of the discharge sequence. The step can be assigned mostly to the KVP electrode, as shown in the Supporting Information (Figure S6a) for a KVP/K half cell (up-shift of the voltage step 200–300 mV).

2.1.2 | *Differential Capacity Analysis*

To illustrate the changes in the voltage profiles over the first 100 cycles, the corresponding dQ/dV plots are also shown in Figure 3 (second depiction in Figure S4). In this version of the dQ/dV analysis, a Savitzky–Golay (SG) filter was applied. Compared to a more basic moving average smoothing (e.g., Jeschull et al. [37]), the SG filter used a third-order polynomial fit with a moving window size of 15 data points (e.g., Köning et al. [38]) (see comparison in Figure S5). In Figure 3, this is reflected by the largely flattened dQ/dV curves in later cycles (>50th cycle), except for the VC-1 sample, which retains most of its profile over the first 100 cycles. In dQ/dV plots of two-electrode full cells, separating individual anode and cathode contributions is challenging without three-electrode data. Therefore, corresponding data from graphite/K and KVP/K half cells are shown in Figure S6 for better comparison. These data show that the dominant dQ/dV features mainly originate from the KVP cathodes and are associated with the sequential V^{3+}/V^{4+} and V^{4+}/V^{5+} redox processes, which lead to multiple redox steps in the upper voltage region and corresponding dQ/dV peaks [19, 20].

From the first to the second charge cycle, a general peak shift can be observed that is associated with changes in the cell resistance such as the additional polarization from the formation of a resistive SEI layer or changing contact resistances. SEI formation causes characteristic voltage step(s) in the low-voltage region, <3.5 V, of the full cell (i.e., in the 0.5–1.5 V region in the voltage profile of the graphite/K half cell), leading to additional features in the first cycle dQ/dV plots: for EC/PC at around 2.7 V, for VC-1 at 3.2 V, and for EC/DEC in the range 2.7–3.4 V. Compared to a moving average approach, the SG filter behaved insensitive to the low-voltage region, even with small window size (see comparison of VC-1 profiles in Figure S3). As indicated in the voltage profiles, the onset of a first voltage step is seen already at about 2.5 V for EC/PC-based electrolytes and 200 mV earlier for EC/DEC. The distinct peak observed for the EC/PC-based electrolytes between 3.5 and 3.7 V is a first-cycle feature of KVP, attributed to a small voltage plateau that shrinks considerably in subsequent cycles.

For all electrolytes, a strong attenuation of peak amplitudes with increasing cycle number is observed, indicating a loss of K-ion inventory due to irreversible reactions. In addition, the two peaks at around 3.9 and 4.0 V gradually merge and shift to higher voltage, while the high-voltage feature at 4.2 V shifts in the opposite direction, toward lower voltage. In general, such

shifts toward higher potentials are assigned to increasing cell resistances and a shifting voltage window in two-electrode full cell configurations (voltage slippage). In a full-cell configuration, loss of cyclable potassium effectively constrains the accessible voltage window to K-lean KVP compositions in the high-voltage region, which may manifest as a straightening of the voltage profile and shifted dQ/dV peak positions. The discharge sequences are more straightforward, with mainly two main features that decrease in peak intensity and shift to lower potentials with increasing number of cycles due to rising cell resistances. The VC-1 sample that retains the profile shape best shows a continuous decrease of these attributes, whereas changes in dQ/dV of other samples occur more sudden.

2.2 | Electrolyte-Dependent Degradation Mechanisms

In the following, a comprehensive degradation analysis is based on samples that were cycle-aged in KVP/graphite cells up to 10 cycles in either of the four electrolytes introduced above. The analysis includes GC/MS experiments, SEM cross sections of graphite electrodes, and XPS analysis of the surface layers formed on graphite electrodes. All samples were prepared and tested in the same manner as presented above in the long-term study. The cycling results over the first 10 cycles are in good agreement with these earlier results, as summarized for the four samples in Table S1.

2.2.1 | Gas Chromatography/Mass Spectrometry Analysis

To study the consumption of additives and the evolution of soluble degradation products, the electrolytes were examined by GC/MS both in their pristine state and in the early stages of SEI formation and growth, i.e., after the first charge, after completion of the first cycle and after 10 cycles (discharged state). The EC/PC and EC/DEC electrolyte systems in Figure 4 are shown as representative examples. The EC/PC samples with additives are shown in Figure S7. In the case of the EC/PC electrolyte, almost no volatile degradation products were observed, except for trace amounts of low-molecular-weight trialkyl phosphate species (namely triethyl phosphate, TEP) detected at a retention time of 13.06 min (see also Figures S9 and S10). This signal was observed exclusively after the first formation cycle and was absent in both the pristine electrolyte and the EC/DEC electrolyte. The transient appearance of TEP was reproduced in several independently prepared samples (Figure S10), confirming that it represents a real intermediate rather than an analytical artifact. Electrolytes containing FEC likewise showed no detectable TEP (detection limit of TEP was about 50–100 ppm in the electrolyte), whereas VC-containing electrolytes exhibited only very small, residual TEP traces, consistent with the altered early-stage SEI chemistry induced by VC (Figures S8–S10). Moreover, it was no longer detected after subsequent cycles. To further confirm its disappearance after the formation cycle, additional samples were analyzed after two and five cycles (Figure S9). The appearance of this species solely during the initial formation cycle therefore suggests that it represents a short-lived intermediate associated with interphase formation. It may be formed via reactions between PF_6^- decomposition products, originating from KPF_6 and solvent decomposition products such as alkoxides that have formed in the initial cycle and may subsequently be incorporated into the interphase or rapidly consumed during further electrochemical processes. To the best of our knowledge, such behavior was not described before.

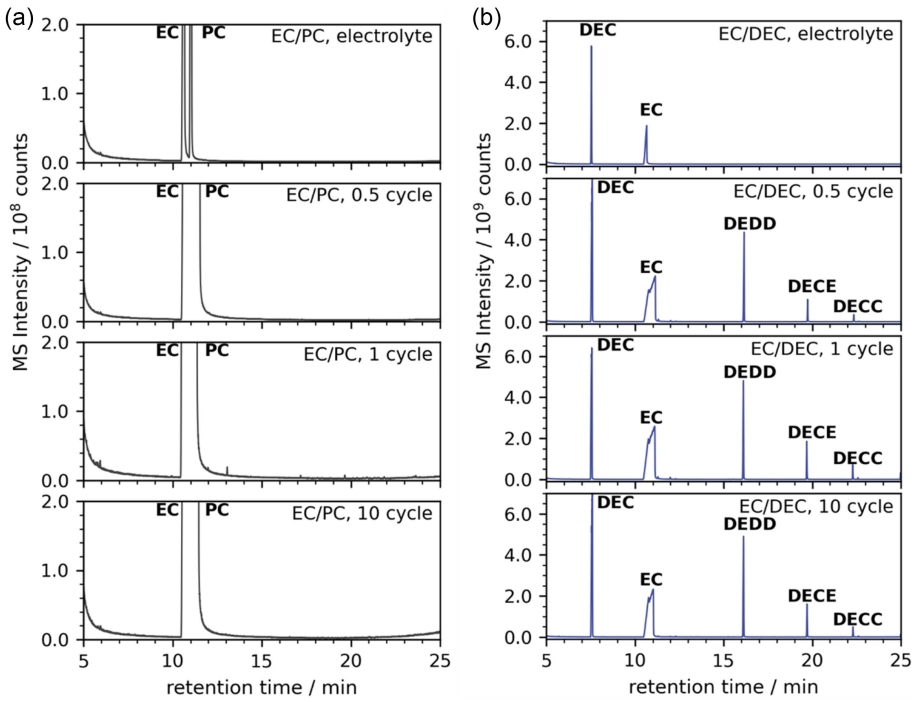

FIGURE 4 | GC/MS measurements from the electrolytes after cell disabling. The (a) EC/PC and the (b) EC/DEC electrolytes are shown as uncycled electrolyte, after 0.5 cycles, after one cycle and after 10 cycles. Prior to the retention time of 5 min, only the argon peak and the dichloromethane solvent were detected.

In contrast, the degradation products formed in the EC/DEC mixture are clearly evident, specifically the dicarbonate derivative DEDD (diethyl 2,5-dioxahexanedioate) bridged by an ethyl chain, the dicarbonate derivative DECE (di-(2-ethoxycarbonyloxyethyl) ether) bridged by an ether group, and the ethyl ether-terminated carbonate DECC (di-(2-ethoxycarbonyloxyethyl) carbonate). Their formation has been observed in earlier studies in the presence of potassium metal [39, 40].

While the analysis was qualitative, relative peak intensities of the decomposition products clearly indicate an increase in their concentration relative to the EC peak during the first cycle. The samples cycled for 10 cycles did not show significantly higher concentrations. When either FEC or VC was used in the EC/PC solvent mixture, no soluble degradation products were found. This suggests that electrolyte decomposition, if present, may predominantly lead to nonvolatile or surface-bound species that cannot be detected by GC/MS. In EC-based electrolyte mixtures, DEC is considerably more susceptible to alkoxide-mediated transesterification reactions than PC, which indicates a higher relative stability of PC toward alkoxide-driven solvent degradation [40].

2.2.2 | *Scanning Electron Microscopy*

Intercalation of K-ions into graphite is known to cause drastic mechanical stress on the material due to the large volume expansion upon forming of the intercalated graphite phases [2, 41–43]. In addition, cointercalation of the solvent was often assigned to cause rapid capacity fade as a consequence of internal decomposition in the cointercalated stage [44, 45]. To further understand the different behaviors of the four full-cell systems and the role of the anode, graphite electrodes were extracted from the cells after 10 cycles and cross-sectional/surface images were obtained with SEM (Figure 5a–h). The cross-sectional images show an inner porosity of the graphite particles with a partial open porosity and pore lengths ranging from 2 to 6 µm. A comparison with the pristine material suggests that the pore dimensions remained largely unchanged. The cross sections reveal charging effects as a peripheral layer surrounding the particles, which are typically attributed to a poor electronically conducting surface layer such as the SEI. Because of the open porosity, electrolyte infiltration and degradation of the particle interior is also occurring, leading to an SEI coverage in the pores of the active material. The SEI morphologies appear individual to every electrolyte system with respect to thickness and material distribution. The most notable difference is seen between EC/PC mixtures and the EC/DEC electrolyte. The latter showed a significantly thicker surface layer. In case of the additive-free EC/PC electrolyte, particle-like features can be seen. However, looking at the top surface image, these features seem to originate more likely from bubbles that have formed in thermal hot spots during the ion milling. Nonetheless, the electron micrograph suggests that the surface layer thickness in this case is still notably higher than in case of electrolyte mixtures with additional amounts of VC or FEC. Compared to the electrolytes without any additives, the top surface images further indicate that VC formed a smooth surface layer over the particles and even interconnected them as can be seen in the contact areas between particles [46]. In case of FEC, small bright spots in the surface layer can be seen in the top surface images, which could be assigned to residual KPF_6 salt that remained after washing, as well as to salt and FEC decomposition products such as KF, according to corresponding EDX maps (Figure S14). Similarly, larger cubic deposits can be seen on the particles surface in the electron micrographs of the EC/DEC sample (Figure 5h) that could be assigned to NaF by correlation with the EDX results (Figure S15). The Na-ion likely originates from sodium carboxymethyl cellulose (CMC-Na) binder. The observed variability in the formation of agglomerated inorganic surface species across different electrolyte systems suggests that the electrolyte composition, particularly the choice of additive or cosolvent, governs the nucleation of inorganic material at the graphite surface. Similar electrolyte-controlled nucleation phenomena have previously been reported for lithium-based systems [47, 48].

The findings of the SEM investigation indicate that the homogeneity of the surface layer as well as its thickness can be correlated with the cycling behavior of the cells, whereby a thick and rough surface layer seems to deteriorate the cyclability. Cross-sectional analyses of the KVP/C cathodes are shown in Figure S16. The particles cycled in the different electrolytes exhibited no significant differences in surface layer formation or morphology; therefore, they are not discussed further.

2.2.3 | *X-ray Photoelectron Spectroscopy*

In order to reveal the composition of the surface layers in the different electrolyte systems, XPS analysis of graphite and KVP/C electrodes was carried out. Due to only marginal changes of

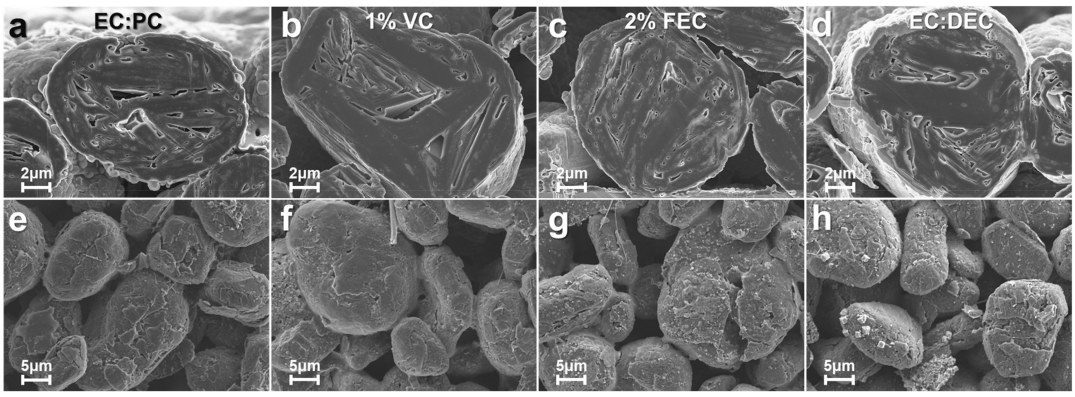

FIGURE 5 | SEM pictures and cross sections of graphite anodes after cycling for 10 cycles in (a,e) EC/PC, (b,f) VC-1, (c,g) FEC-2, and (d,h) EC/DEC electrolytes.

the CEI layers after charge and discharge, the spectra are only briefly discussed herein and are shown in Figures S20 and S21. C1s/K2p and O1s/V2p spectra of the graphite electrodes after the first half- and full-cycle are shown in Figure 6a–d. In some of the F1s and P2p spectra, noticeable BE shifts were observed when comparing spectra with and without charge compensation. For example, Figure S18 shows a shift of ≈0.2 eV in the F1s spectrum of the initially charged graphite electrode. In this regard, charge-compensated spectra were used for discussion herein.

2.2.3.1 | *C1s/K2p Core-Level Spectra.* In the C1s/K2p region, peaks are assigned to the sp^2 graphite peak at ≈283.3 eV, the hydrocarbon/adventitious carbon peak at 285 eV (used for referencing of all spectra), as well as oxidized carbon species attributed to –C–O–/–C–OK (≈286 eV), –C=O (≈287.8 eV), –(C=O)OR/K_2CO_3 (≈288.8 eV), and organic carbonates (≈289.9 eV). In the K2p region, inorganic K-species such as KF and K_2CO_3 as well as organic compounds like ROK show up as a broad $2p_{3/2}$ peak at ≈293.3 eV. With VC as additive, additional peaks can be found at ≈290.8 eV, which can be assigned to poly(VC) [49,–51]. The curve shape of the K2p region suggests the splitting of the K-species [32], as even broadening of the fitted peaks (for example, suggested by Oswald et al. [52]) did not properly match the measured data. Therefore, a second compound was fitted at a $2p_{3/2}$ peak position of ≈294.3 eV, which may be assigned to higher oxidized K-species (e.g., $K_xPO_yF_z$). Inferring from the small sp^2-peak intensities of the bulk graphite signal, comparatively thick SEI layers can be observed for the EC/PC-based electrolytes at the end of the first charge already. After the first cycle, the signal disappeared almost entirely. The behavior was slightly different for the EC/DEC electrolyte, where the sp^2 peak remained prominent after the first charge, indicating initially a thinner SEI. However, after completing the first cycle the sp^2 peak was barely visible in the spectrum, similar to the other samples. Interestingly, there is also a fundamental change in the SEI composition, when comparing the relative peak ratios between the C1s species and the K2p doublet: Based on the peak areas of the hydrocarbon (sp^3-C) peak and $K2p_{3/2}$ peaks, the graphite surface exhibits a high surface content of potassium after the first charge in electrolytes with EC/PC. After completing the first cycle, the hydrocarbon peak increased significantly, indicating the deposition of more organic compounds on the electrode surface, and thus a change in the elemental distribution of the surface composition with a decreasing potassium content. Furthermore, K-species become more clearly visible in the K2p spectrum of the EC/PC-based electrolytes. The EC/DEC electrolyte behaves differently, as the relative peak intensities between hydrocarbon and K2p signal remained similar between the two stages of aging. It is further observed that the oxidized carbon species increase notably in intensity. It should be stressed that the compositional change in all samples occurs within the first cycle, while the SEI continues to grow. Hence, while the absolute amount of potassium may still increase during this time, its relative mass fraction in the SEI decreases.

O1s-V2p core-level spectra. In the O1s spectra obtained after a half- and full-cycle, mainly three peaks can be identified which correspond to –C=O/–CO_x (≈531 eV), –C–O– (≈532.6 eV) and –C–OK (≈533.9 eV) components. Conspicuously, for the EC/DEC system, a peak doublet can be identified in the V2p region ($2p_{3/2}$ peak at ≈516.8 eV) which most likely corresponds to V^{3+} species, as similarly described by Larhrib et al. [32] for the KVPOF system. This strongly suggests dissolution and subsequent migration of vanadium from the cathode to the opposite electrode, which is also confirmed by EDX (see Figure S15h). The loss of the redox-active species from the active cathode material is likely a contributing factor to the rapid performance decay observed for the EC/DEC system.

2.2.3.2 | *F1 and P2p Core-Level Spectra.* The spectra of both core levels are provided in the Supporting Information (Figure S17). Most spectra show a (unreacted) $PF6^-$ component at 687.0 eV,

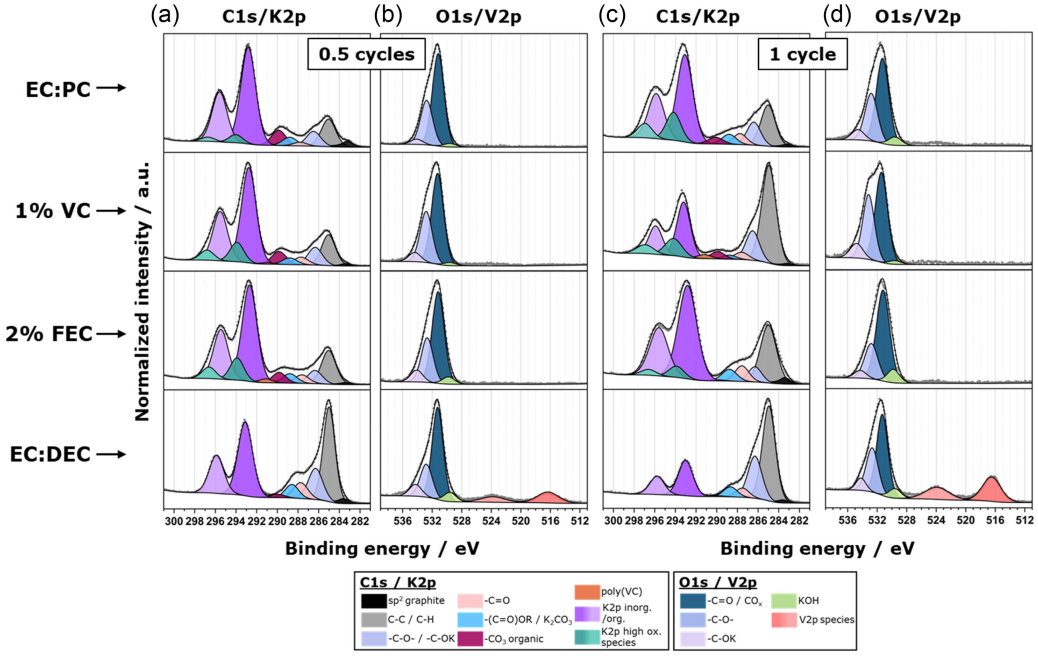

FIGURE 6 | C1s/K2p and O1s/V2p XPS spectra of graphite anodes cycled in different electrolytes after initial (a,b) charge and (c,d) discharge.

possibly as salt inclusions in the SEI or residues that were not fully washed off the surface. KF is located at low BEs between 283.4 and 284.0 eV. The BE of both components is in agreement with previously reported values [3, 4, 53]. The corresponding PF_6^- signal (138.0 eV) in the P2p spectra can only be clearly seen for the EC/DEC electrolyte and for EC/PC after a full charge–discharge cycle. For EC/DEC and FEC-2 (discharge), a second P component that is typically assigned to phosphate species, e.g., $O=PF_x(OR)_y$, is observed at 134.0 eV in the P2p and at around 685.0 eV in the F1s spectra. The F1s spectra suggest small amounts of this compound also in the spectra of the charged state for VC-1 and EC/PC, that are below the detection limit in the corresponding P2p spectra. The F and P contents of surface layers formed in VC-1 appeared particularly low after one cycle (based on XPS measurements on different spots on the sample). Interestingly, in the spectrum of the DEC system, a peak at 684.3 eV indicates the formation of NaF, which is further confirmed by the Na1s spectrum (Figure S19), and is also in agreement with the EDX findings discussed before (Figure S15). After the first discharge, the formation of organic fluoro-species (BE at 689.2 eV) can be seen in the FEC-2, which is commonly observed in carbonate-based electrolytes with FEC [37, 54].

2.2.3.3 | *Potassium Vanadium Phosphate Cathode Surface Layer.* The XPS spectra of the KVP/C electrodes after first charge and discharge (Figures S20 and S21) do not show significant changes, despite indicating a slight increase of salt over solvent decomposition. It can also be observed that for EC/PC and VC-1 electrolytes, more K2p species formed on the surface.

2.2.3.4 | *Elemental Distribution.* Figure 7 depicts the changes of surface species atomic concentrations (given in at.%) between first charge and discharge of the graphite electrodes in the four electrolytes (obtained from the ratio between the normalized peak area/sum of normalized peak areas with the inclusion of instrument-specific sensitivity factors). Based on previous results [3], there is a high risk that the SEI layer thickness exceeds the probing depth using in-house XPS (≈5–10 nm). Because of this limitation, the quantification may not refer to the entire surface layer but only the topmost fraction, within the probing volume. It can be seen that for all PC-containing electrolytes, the total amount of the carbon species are virtually similar in the first charge cycle, although with notable differences between the individual components on SEI formed in EC/PC-based electrolytes. The fluorine and phosphorous core levels are comparatively minor components in the surface layer formed on the graphite electrodes, accounting for less than 7 at.% F species and <1 at.% P species (Tables S2 and S3). Accordingly, the F1s and P2p spectra are both weak signals by comparison. In fact, among the charged samples, only EC/DEC shows a measurable P2p signal. Furthermore, the fluorine content in the SEI formed in the VC-1 electrolyte, predominantly originating from KF formation in this case, is about twice as high than for EC/PC formulation and slightly higher than for the FEC-2 system. However, differences in the degree of salt degradation and KPF_6 inclusions are negligible after first charge. In contrast, the results suggest distinct differences to the EC/DEC electrolyte, with not only notably lower K-salt contents (and no KF) but also a larger organic fraction (specifically hydrocarbon). The amount of detected vanadium

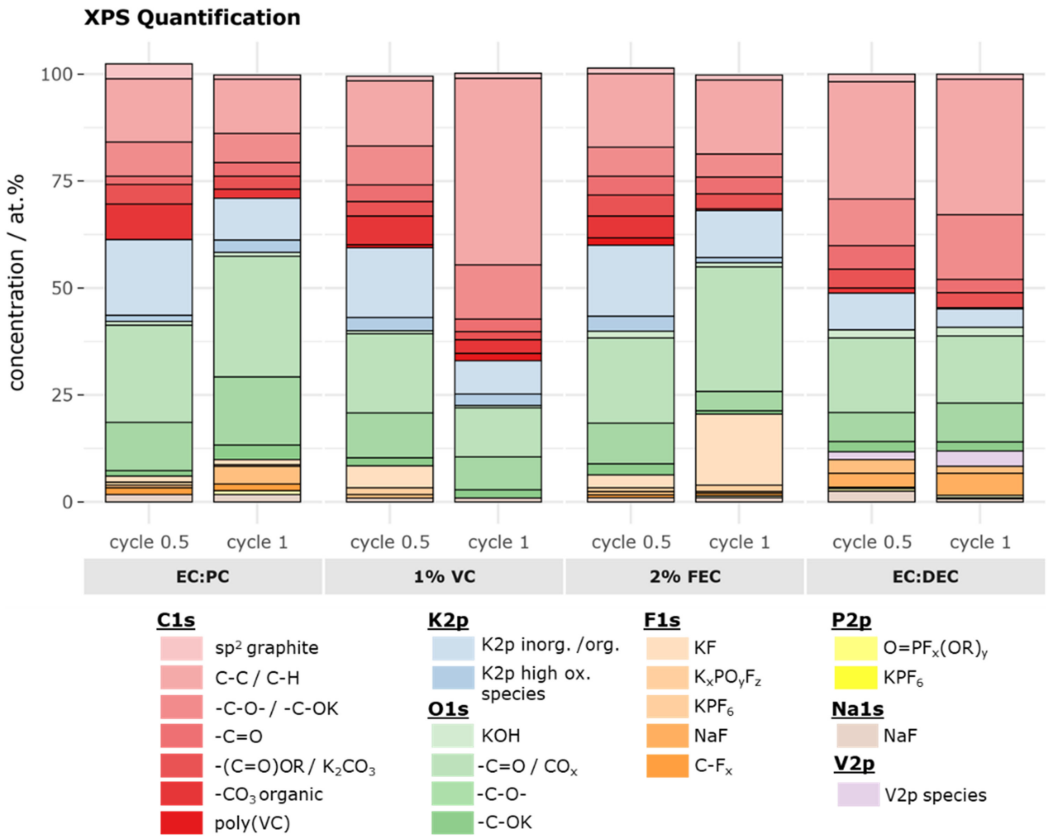

FIGURE 7 | Bar plots showing the evolution of surface species atomic concentrations on graphite electrodes cycled in different electrolytes after first charge and discharge. Values are derived from peak fitting of core-level spectra.

species that were only found for the EC/DEC formulation is about 1.8 at.%.

Stronger variation between the four systems is observed after discharge. While for the EC/PC and FC-2 formulations the organic carbon/oxygen fractions are visually decreasing, it is significantly increasing for the VC-1 formulation. Concurrently, the inorganic fraction is reduced to an extend close to the detectability threshold, while for the other two PC systems it is increasing. Between the EC/PC and FEC-2 formulation, the inorganic fraction differs in the amount of KF, which remains on a moderate level for the EC/PC formulation while it is drastically increased for the FEC-2 system. Similar trends in the three systems are exclusively seen for the evolution of K2p species which shows a general reduction of the concentrations. The EC/DEC system also shows an increase of the organic carbon/oxygen fraction and, albeit only marginal, increase of inorganic fluorine species such as NaF/KF after discharge. In addition, continuous dissolution of vanadium species is indicated by a further increase of the concentrations to ≈3.5 at.%.

A quantification was also performed after the 10th cycle and is shown in Figure S24 (respective spectra are shown in Figures S22 and S23). The C1s spectrum indicates an increased contribution from organic species, while inorganic fluorine species in the F1s become less dominant. In addition, the K2p signals show a general increase for all four systems, with the most pronounced rise observed for the FEC-2 and EC/DEC systems.

3 | Discussion

In this work, graphite/KVP two-electrode cells with sensible electrode balancing (N/P ≈0.9) were used for electrolyte studies on full cells. As our previous work demonstrated, the SEI formation, its composition, and thickness can be fundamentally different in half cell experiments with a potassium counter electrode [4]. Electrolyte studies performed in half cells are thus biased due to the high reactivity of potassium toward electrolyte component. For more tangible results on the stability and benefit of different solvent mixtures and electrolyte additives, tests in full cell configurations therefore become a necessity for KIBs. To illustrate the impact of this issue, we herein selected four different electrolyte compositions, including VC and FEC as additives. At an additive content of 1 vol.% VC provided a trade-off between sufficient surface passivation and excessive decomposition and interphase growth, while any amount of FEC was detrimental to the capacity retention. Coin cell setups like the one in this work use comparatively high electrolyte amounts, i.e., small electrode loading to electrolyte volume ratios, leading to rather cell-specific optimum values. Therefore, in other cell configurations (e.g., pouch cells) [55] varying optimum amount can be expected, while the overarching trends between additives should remain unaffected. Especially for the use of FEC, contradicting results are reported. Ells et al. [56] referred the detrimental effects of FEC to the high reactivity of the additive with potassium, thus forming insulating KF passivation layers. According to Liu et al. [57], FEC had detrimental impact on graphite/K half cells. In contrast, in cathode/K half cells, FEC and VC appear to have a stabilizing effect compared to additive-free electrolytes [25, 58]. Previous works illustrated this issue with the additive DTD (1,3,2-dioxathiolane 2,2-dioxide) which passivates K-metal, but is poorly compatible with graphite [26, 27].

The choice of graphite in this work allowed the use of EC/PC mixtures, which normally leads to graphite exfoliation in many types of graphite. EC/PC-based electrolytes come with the benefit of higher anodic stability (Kim et al. [36]) and they avoid the formation of bis(alkyl carbonates) that were associated previously with cross talk and parasitic reactions [27, 40, 59]. This was confirmed in the systems investigated herein by GC/MS experiments. Interestingly, small amounts of TEP were detected in EC/PC-based systems (except when FEC was present). In addition, our XPS study showed that EC/PC-based electrolytes also suppressed the cross talk of vanadium, that was only found on the graphite surface when EC/DEC was used. Further analysis on the graphite aging suggested that in the presence of VC, a polymer is formed at the surface that interconnects interparticle gaps, avoids particle fracture, and excessive surface layer growth. This is also reflected in the XPS results, by a significantly more intense hydrocarbon component (possibly due to polymer at the surface) and overall a less inorganic surface layer composition. In this regard, the XPS results in this work are in line with previous in-house XPS results on graphite/K half cells and hard XPS experiments on graphite/$K_2Fe[Fe(CN)_6]$ full cell results, both in the same EC/DEC electrolyte formulation [3, 4]. In agreement with the latter full cell study, it can also be concluded that inorganic fluorine and phosphorus species, arising from salt decomposition, appear to play a minor role in SEI formation, suggesting that other decomposition pathways (mainly involving organic species) dominate interphase chemistry under full-cell operating condition. However, it is also demonstrated that for vanadium-phosphate-based polyanionic systems the application of DEC-containing electrolytes can have detrimental influence on cycling behavior except showing similar initial SEI formation, which can be explained by the strong tendency to dissolve both organic and vanadium species, thus causing electrode cross talk, and thereby actively damaging the cathode active material as well as the anode protective surface layer. XPS after 10 cycles (Figure S23) further revealed the increase of potassium species, which correlates the loss of K-ion inventory to the observed capacity fade of the cells. As the increase in the K2p is accompanied with an increase of the organic carbon fraction, it can be assumed that the newly formed K-species are, in contrast to the initial cycle, mostly of an organic nature.

Potassium salts in general, and organic salts in particular, tend to be more soluble than corresponding lithium and sodium salts (in the general order Li (least soluble) < Na < K) [60, 61]. Soluble salts may be considered active K-inventory (insoluble species would be considered inactive K-inventory) [62], which can provide an explanation as to why the low initial Coulombic efficiencies do not lead to faster capacity fade. According to Holtstiege et al. [62], several parasitic reactions, including electropolymerization (as expected for VC), H_2 formation and metal dissolution and redeposition, as well as redox shuttle mechanisms, do not consume the active charge carrier inventory but lower the C.E. Moreover, it should be stressed that the comparatively large electrolyte reservoir may partially buffer K-ion losses in coin cell configurations. This effect is expected to become less pronounced under more electrolyte-lean and application-relevant cell setups

(such as pouch cells), where the available potassium inventory is more tightly constrained.

4 | Conclusion

In this study, we demonstrated cycling results of KVP/C ‖ graphite full cells with different liquid electrolyte formulations. The standard electrolyte composition 0.5 M KPF_6 EC/PC (1:1) showed a comparably solid performance, given the known compatibility issues of PC and graphite. Addition of 1% of VC could significantly improve the capacity retention of the full cell, while the use of FEC as additive and DEC as PC substitute demonstrated detrimental effects on cycle life. SEM and XPS investigations further revealed the formation of initially organic/polymeric dominated SEIs on the graphite anodes with only minor amounts of inorganic salt decomposition compounds. It was deduced that generally more stable cycling behavior can be expected with this particular interface constellation. This work highlights the importance of electrolyte design strategies in KVP-based systems in order to enable long-lasting K-ion full cells.

5 | Experimental Section

5.1 | Materials

Potassium hexafluorophosphate (KPF_6, ≥99%, Sigma-Aldrich) was dried at 120°C for 12 h in vacuo (10^{-3} mbar) prior to use.

Ethylene carbonate (EC, 99%, Alfa Aesar), propylene carbonate (PC, 99.7%, Sigma-Aldrich), diethyl carbonate (DEC, ≥99%, Sigma-Aldrich), vinylene carbonate (VC, 98%, Fisher Scientific), fluoroethylene carbonate (FEC, ≥99%, Sigma-Aldrich), graphite (C-NERGY ACTILION GHDR15-4, Imerys Graphite & Carbon Switzerland), carbon black (CB, Super C Imerys Graphite & Carbon Switzerland), poly(vinylidene fluoride) (PVdF, Solef 6020/1001, Solvay), sodium carboxymethyl cellulose (Na-CMC, Sigma-Aldrich), poly(acrylic acid) (PAA, $M_v \approx 1.25$ Mio., Sigma-Aldrich), and *N*-methyl-2-pyrrolidone (99.5%, Sigma-Aldrich) were used as received (Karl Fisher titration of the carbonate solvents and the respective electrolytes confirmed water contents below 10 ppm. Furthermore, GC/MS was conducted of the solvents, additives, and prepared electrolyte to confirm purity).

The synthesis of potassium vanadium phosphate composites ($K_3V_2(PO_3)_4$, KVP/C) by a spray-drying method and the corresponding characterization (including XRD and half cell cycling data) is described in a previous study by our group [21].

5.2 | Cell Assembly and Electrochemical Analysis

5.2.1 | *Electrode Preparation*

KVP/C electrodes were prepared by mixing KVP/C active material, carbon black (CB), and PVdF in a ratio of 8:1:1 in NMP and by doctor blading the obtained slurry on Al foil to a wet thickness of 200 µm.

Graphite electrodes were similarly produced by mixing Actilion graphite powder, CB, Na-CMC, and PAA in a ratio of 95:1:2:2 in deionized water and by doctor blading the slurry on Cu foil. The wet thickness of the coating was fixed to 50 µm to balance cathode/anode capacities.

Both KVP/C and graphite electrodes were obtained by cutting discs of 12 and 14 mm diameters, respectively. The electrodes were dried at 80°C in a climate chamber overnight, followed by drying at 120°C under vacuum (10^{-3} mbar). The final mass loading of the dried KVP/C electrodes was ≈4.9 mg cm^{-2} and of the dried graphite electrodes ≈1.9 mg cm^{-2}. Referring to the theoretical capacities of KVP/C and graphite ($Q_{KVP/C} = 106$ mAh g^{-1}; $Q_{graphite} = 279$ mAh g^{-1}), the N/P ratio was ≈0.9 (note different electrode sizes). The electrodes were then stored in an Ar-filled glovebox and further used without exposure to air.

5.2.2 | *Electrolyte Preparation*

Base electrolyte 0.5 M KPF_6 EC/PC was prepared by dissolving KPF_6 in an EC/PC 1:1 mixture. 0.5 M KPF_6 EC/DEC electrolyte (1:1 ratio of EC/DEC) was prepared likewise. The electrolytes with additives FEC and VC were prepared by adding appropriate amounts of the additives to the base electrolyte (numbers in the abbreviations indicate vol.% of the additive).

5.2.3 | *Cell Assembly*

For cell tests, coin cells were assembled in an Ar-filled glovebox. Specifically, in full-cell case, 12 mm KVP/C cathode, 14 mm graphite anode, 150 µL of electrolyte, and 16 mm Whatman separator were inserted into a two-electrode coin cell setup. In half-cell setup, the respective electrode was paired with a 14-mm potassium electrode on Cu foil, 150 µL of electrolyte, and a 16-mm Whatman separator.

5.2.4 | *Galvanostatic Cycling*

Galvanostatic cycling with potential limitation (GCPL) was conducted on a multichannel VMP3 potentiostat (BioLogic Science Instruments) at 25°C in a climate chamber. The coin cells were charged and discharged using a constant current which was calculated according to electrode mass and theoretical capacity of KVP (106 mAh g^{-1}) as well as a cycling rate of C/20. In addition, a constant potential step was added after each charge/discharge cycle for 30 min with a current limitation of half the initial applied current. The cells were cycled for minimum 100 cycles or until they reached 50% capacity loss. In full-cell setup, the voltage range was set from 2–4.4 V, whereas in half-cell setup, the upper potential was increased to 4.5 V. The voltage window was defined on the basis of KVP half-cell data (differential capacity (dQ/dV) analysis) [21]. The upper cutoff was set deliberately in a narrow range to include the high-redox feature at 4.4 V (vs. K^+/K), but to avoid voltage drifts into higher potential regions, as well to mitigate the risk of potassium plating at the graphite negative electrode. For rate capability tests, the cycling rate was changed after every 10th cycle and ranged from C/20 to C/2.

5.2.5 | *Potentiostat Data Generating and Processing*

GCPL data were exported using EC-Lab software (V11.61, BioLogic). All data processing was carried out in R (version 4.5.0), using the data "bat2dat" processing workflow [63]. A script

(in R) for differential capacity analysis was generated with support of ChatGPT (version GPT-5.1) and selected cycles were analyzed by two different approaches: a) using a SG differentiation and b) a finite-difference approach in combination with a moving average. Further details and a comparison of the two approaches are shown in Figure S2.

5.3 | Additional Characterization Methods

5.3.1 | Gas Chromatography/Mass Spectroscopy

GC/MS experiments were carried out according to the previously described method [39]. In brief, a Clarus 690 GC device (PerkinElmer Inc., Waltham, USA) equipped with a 5 MS Sil capillary column and a MS detector (SQ8T) was used for the measurement. The separator sheets were extracted with dichloromethane and the diluted solvent was cleaned through a syringe filter before measurement. The Turbomass 6.1.2 software packages were utilized for data acquisition and subsequent analysis.

5.3.2 | Scanning Electron Microscopy with Energy-Dispersive X-ray Analysis

SEM was carried out on a Merlin GEMINI microscope (Zeiss) and EDX analysis was conducted using an EDX XamN detector (Oxford instruments). Cross sections of graphite electrodes were obtained by ion milling with a PECS II precision etching system (Gatan).

5.3.3 | X-ray Photoelectron Spectroscopy

Prior to XPS analysis, the cells were opened under argon atmosphere in a glovebox. The electrodes were extracted and then washed in 1 ml PC for 45 s and dried by evaporating the solvent. Half of the washed electrodes were adhered to the sample holder using conductive copper tape. The sample holder was then transferred to the spectrometer under argon atmosphere.

XPS was conducted on a K-alpha spectrometer (Thermo Fisher Scientific, East Grinstead, UK) using monochromatic, microfocused Al-K_α X-ray source ($h\nu = 1486.6$ eV) with 400 µm spot size and a pass energy of 50 eV. The Thermo Avantage software (version 6.8.1, Thermo Scientific) was used for data acquisition and processing. To minimize localized charging effects, an electron flood gun with low-energy electrons (8 eV) was used in KVP/C samples while graphite samples were measured without charge compensation. To ensure reproducibility, three spots were measured on each sample. Referencing was realized by shifting all spectra to the hydrocarbon C1s peak at 285 eV, and for comparability, the spectra were normalized to the maximum peak height of 1. A Shirley-type ("smart background") and Voigt profiles with 70% Gaussian and 30% Lorentzian contribution were used for peak fitting. The graphite peak (sp^2 peak) was fitted asymmetrically with a tail mix: 75% and tail exponent: 0.02 for graphite electrodes and tail mix: 75% and tail exponent: 0.4 for KVP/C electrodes. For quantification the analyzer transmission function and Scofield sensitivity factors were applied.

Author Contributions

Celine Röder: investigation, writing – original draft, methodology, writing – review and editing, formal analysis, data curation, validation, visualization. **Ulf-Christian Rauska:** investigation, writing – original draft, methodology, writing – review and editing, formal analysis, data curation, visualization, validation. **Andreas Hofmann:** investigation, writing – original draft, methodology, formal analysis, validation, writing – review and editing, data curation. **Andreas Heyn:** investigation, writing – review and editing, methodology. **Valeriu Mereacre:** investigation, methodology, writing – review and editing. **Joachim R. Binder:** conceptualization, writing – review and editing, project administration, supervision, resources. **Fabian Jeschull:** resources, supervision, project administration, writing – review and editing, writing – original draft, conceptualization.

Acknowledgments

This work contributes to the research performed at CELEST (Center for Electrochemical Energy Storage Ulm-Karlsruhe) and was funded by the German Research Foundation (DFG) under Project ID 390874152 (POLiS Cluster of Excellence).

Open Access funding enabled and organized by Projekt DEAL.

Funding

The study was supported by Deutsche Forschungsgemeinschaft (390874152).

Conflicts of Interest

The authors declare no conflicts of interest.

Declaration of Generative AI and AI-Assisted Technologies in the Writing Process

During the preparation of this work, the authors used ChatGPT-5.1 to assist the development of the R scripts to automate plotting of differential capacity and voltage profile data, including routines for normalizing, reshaping, filtering and smoothing of the raw data. After using this tool, the authors reviewed and edited the content as needed and take full responsibility for the content of the published article.

Data Availability Statement

The data to the above-presented findings are openly available on Zenodo online repository under https://doi.org/10.5281/zenodo.19603859.

References

1. S. Komaba, T. Hasegawa, M. Dahbi, and K. Kubota, "Potassium Intercalation into Graphite to Realize High-Voltage/High-Power Potassium-Ion Batteries and Potassium-Ion Capacitors," *Electrochemistry Communications* 60 (2015): 172–175, https://doi.org/10.1016/j.elecom.2015.09.002.

2. J. Zhao, X. Zou, Y. Zhu, Y. Xu, and C. Wang, "Electrochemical Intercalation of Potassium into Graphite," *Advanced Functional Materials* 26, no. 44 (2016): 8103–8110, https://doi.org/10.1002/adfm.201602248.

3. F. Allgayer, J. Maibach, and F. Jeschull, "Comparing the Solid Electrolyte Interphases on Graphite Electrodes in K and Li Half Cells," *ACS Applied Energy Materials* 5, no. 1 (2022): 1136–1148, https://doi.org/10.1021/acsaem.1c03491.

4. F. Jeschull, E. Kataev, I. Panasenko, C. Njel, R. Félix, and J. Maibach, "Why Half-Cell Samples Provide Limited Insight Into the Aging

Mechanisms of Potassium Batteries," *Advanced Energy Materials* 12 (2025): 2403811, https://doi.org/10.1002/aenm.202403811.

5. F. Jeschull and J. Maibach, "Inactive Materials Matter: How Binder Amounts Affect the Cycle Life of Graphite Electrodes in Potassium-Ion Batteries," *Electrochemistry Communications* 121 (2020): 106874, https://doi.org/10.1016/j.elecom.2020.106874.

6. Z. Jian, W. Luo, and X. Ji, "Carbon Electrodes for K-Ion Batteries," *Journal of the American Chemical Society* 137, no. 36 (2015): 11566–11569, https://doi.org/10.1021/jacs.5b06809.

7. G. He and L. F. Nazar, "Crystallite Size Control of Prussian White Analogues for Nonaqueous Potassium-Ion Batteries," *ACS Energy Letters* 2, no. 5 (2017): 1122–1127, https://doi.org/10.1021/acsenergylett.7b00179.

8. K. Hurlbutt, S. Wheeler, I. Capone, and M. Pasta, "Prussian Blue Analogs as Battery Materials," *Joule* 2, no. 10 (2018): 1950–1960, https://doi.org/10.1016/j.joule.2018.07.017.

9. Y. Matos-Peralta and M. Antuch, "Review—Prussian Blue and Its Analogs as Appealing Materials for Electrochemical Sensing and Biosensing," *Journal of the Electrochemical Society* 167, no. 3 (2019): 037510, https://doi.org/10.1149/2.0102003JES.

10. L. Li, Z. Hu, Q. Liu, J.-Z. Wang, Z. Guo, and H.-K. Liu, "Cathode Materials for High-Performance Potassium-Ion Batteries," *Cell Reports Physical Science* 2, no. 12 (2021): 100657, https://doi.org/10.1016/j.xcrp.2021.100657.

11. T. Masese and G. M. Kanyolo, "Advancements in Cathode Materials for Potassium-Ion Batteries: Current Landscape, Obstacles, and Prospects," *Energy Advances* 3, no. 1 (2024): 60–107, https://doi.org/10.1039/D3YA00406F.

12. C. Vaalma, D. Buchholz, and S. Passerini, "Non-Aqueous Potassium-Ion Batteries: A Review," *Current Opinion in Electrochemistry* 9 (2018): 41–48, https://doi.org/10.1016/j.coelec.2018.03.031.

13. T. Hosaka, T. Shimamura, K. Kubota, and S. Komaba, "Polyanionic Compounds for Potassium-Ion Batteries," *Chemical Record* 19, no. 4 (2019): 735–745, https://doi.org/10.1002/tcr.201800143.

14. X. Sheng, J. Liao, Z. Yuan, et al., "Synergy of Phase and Interface Engineering of Manganese Difluoride Enables High-Efficiency Potassium-Ion Batteries," *Energy & Environmental Science* 18, no. 11 (2025): 5407–5415, https://doi.org/10.1039/D5EE00499C.

15. Z. Wang, K. Luo, J.-F. Wu, et al., "Rejuvenating Propylene Carbonate-Based Electrolytes by Regulating the Coordinated Structure toward All-Climate Potassium-Ion Batteries," *Energy & Environmental Science* 17, no. 1 (2024): 274–283, https://doi.org/10.1039/D3EE03340F.

16. Y. Mo, W. Zhou, S. Wu, et al., "Polarity Gradient CEI Driven Rapid Desolvation for Extreme Fast-Charging Potassium-Ion Batteries," *Angewandte Chemie International Edition* 64, no. 48 (2025): e202518712, https://doi.org/10.1002/anie.202518712.

17. Z. Yuan, L. Chen, J. Liao, et al., "Methyl Asymmetric Interference-Enhanced Dipole–Dipole Interaction for High-Performance Potassium–Graphite Battery Electrolyte Design," *Angewandte Chemie International Edition* 65, no. 12 (2026): e23473, https://doi.org/10.1002/anie.202523473.

18. H. Qi, Y. Du, J. Ding, et al., "Regulating Interface Electric Field to Stabilize High-Voltage KVPO4F Positive Electrode for Sustainable Potassium-Ion Batteries," *Nature Communications* 17 (2026), https://doi.org/10.1038/s41467-026-71647-x.

19. J. Han, G.-N. Li, F. Liu, et al., "Investigation of $K_3V_2(PO_4)_3$/C Nanocomposites as High-Potential Cathode Materials for Potassium-Ion Batteries," *Chemical Communications* 53, no. 11 (2017): 1805–1808, https://doi.org/10.1039/C6CC10065A.

20. H.-X. Kuai, J.-F. Lu, X.-Y. Lv, Jing-Su, Y.-F. Long, and Y.-X. Wen, "Three-Dimensional and Porous K3V2(PO4)3/C Cathode Material for Potassium-Ion Batteries," *Ionics* 28, no. 8 (2022): 3817–3831, https://doi.org/10.1007/s11581-022-04612-5.

21. A. Heyn, C. Röder, H. Geßwein, et al., "Hierarchical Microstructured K3V2(PO4)3/C-Composite Electrode for Potassium-Ion-Batteries Through Scalable Spray-Drying Approach," *ChemSusChem* 18 (2025): e202501111, https://doi.org/10.1002/cssc.202501111.

22. T. Hosaka and S. Komaba, "Development of Nonaqueous Electrolytes for High-Voltage K-Ion Batteries," *Bulletin of the Chemical Society of Japan* 95, no. 4 (2022): 569–581, https://doi.org/10.1246/bcsj.20210412.

23. L. Fan, H. Xie, Y. Hu, et al., "A Tailored Electrolyte for Safe and Durable Potassium Ion Batteries," *Energy & Environmental Science* 16, no. 1 (2023): 305–315, https://doi.org/10.1039/D2EE03294E.

24. Y. Liu, C. Gao, L. Dai, et al., "The Features and Progress of Electrolyte for Potassium Ion Batteries," *Small* 16, no. 44 (2020): 2004096, https://doi.org/10.1002/smll.202004096.

25. N. Dautain, J.-F. Martin, D. Sotta, P. Azais, and D. Peralta, "The Tremendous Challenge of Suitable KPF6-Based Electrolytes for 4 V-Class K-Metal Cells," *Journal of Power Sources* 614 (2024): 234993, https://doi.org/10.1016/j.jpowsour.2024.234993.

26. T. Hosaka, T. Fukabori, T. Matsuyama, R. Tatara, K. Kubota, and S. Komaba, "1,3,2-Dioxathiolane 2,2-Dioxide as an Electrolyte Additive for K-Metal Cells," *ACS Energy Letters* 6, no. 10 (2021): 3643–3649, https://doi.org/10.1021/acsenergylett.1c01238.

27. I. Panasenko, M. Bäuerle, and F. Jeschull, "How Reference Electrodes Improve Our Understanding of Degradation Processes in Half and Full Cell Potassium-Ion Battery Setups," *Electrochimica Acta* 513 (2025): 145551, https://doi.org/10.1016/j.electacta.2024.145551.

28. S. Baek, S. Jie, and B. Lee, "Effects of Fluoroethylene Carbonate Additive on Potassium Metal Anode," *Journal of Mechanical Science and Technology* 37, no. 7 (2023): 3657–3665, https://doi.org/10.1007/s12206-023-0630-3.

29. S. U. Yoon, H. Kim, H.-J. Jin, and Y. S. Yun, "Effects of Fluoroethylene Carbonate-Induced Solid-Electrolyte-Interface Layers on Carbon-Based Anode Materials for Potassium Ion Batteries," *Applied Surface Science* 547 (2021): 149193, https://doi.org/10.1016/j.apsusc.2021.149193.

30. D. Aurbach, K. Gamolsky, B. Markovsky, Y. Gofer, M. Schmidt, and U. Heider, "On the Use of Vinylene Carbonate (VC) as an Additive to Electrolyte Solutions for Li-Ion Batteries," *Electrochimica Acta* 47, no. 9 (2002): 1423–1439, https://doi.org/10.1016/S0013-4686(01)00858-1.

31. M. Nie, J. Demeaux, B. T. Young, et al., "Effect of Vinylene Carbonate and Fluoroethylene Carbonate on SEI Formation on Graphitic Anodes in Li-Ion Batteries," *Journal of the Electrochemical Society* 162, no. 13 (2015): A7008–A7014, https://doi.org/10.1149/2.0021513jes.

32. B. Larhrib, L. Madec, L. Monconduit, and H. Martinez, "A Novel K-Ion KVPO4F0.5O0.5/Graphite Full Cell: Correlation between XPS SEI Studies and Electrochemical Testing Results," *Journal of Power Sources* 588 (2023): 233743, https://doi.org/10.1016/j.jpowsour.2023.233743.

33. R. Petibon, E. C. Henry, J. C. Burns, N. N. Sinha, and J. R. Dahn, "Comparative Study of Vinyl Ethylene Carbonate (VEC) and Vinylene Carbonate (VC) in $LiCoO_2$/Graphite Pouch Cells Using High Precision Coulometry and Electrochemical Impedance Spectroscopy Measurements on Symmetric Cells," *Journal of the Electrochemical Society* 161, no. 1 (2013): A66–A74, https://doi.org/10.1149/2.030401jes.

34. Y. Qian, C. Schultz, P. Niehoff, et al., "Investigations on the Electrochemical Decomposition of the Electrolyte Additive Vinylene Carbonate in Li Metal Half Cells and Lithium Ion Full Cells," *Journal of Power Sources* 332 (2016): 60–71, https://doi.org/10.1016/j.jpowsour.2016.09.100.

35. X. Liu, M. Zhang, R. Ping, Y. Chen, and X. Hu, "A Study on the Effects of Vinylene Carbonate and Fluoroethylene Carbonate on Thermal Runaway in Lithium-Ion Batteries," *Journal of Power Sources* 649 (2025): 237428, https://doi.org/10.1016/j.jpowsour.2025.237428.

36. H. Kim, Y. Tian, and G. Ceder, "Origin of Capacity Degradation of High-Voltage $KVPO_4$ F Cathode," *Journal of the Electrochemical Society* 167, no. 11 (2020): 110555, https://doi.org/10.1149/1945-7111/aba54e.

37. F. Jeschull, F. Lindgren, M. J. Lacey, F. Björefors, K. Edström, and D. Brandell, "Influence of Inactive Electrode Components on Degradation Phenomena in Nano-Si Electrodes for Li-Ion Batteries," *Journal of Power Sources* 325 (2016): 513–524, https://doi.org/10.1016/j.jpowsour.2016.06.059.

38. L. Köning, J. Göhmann, and P. Bilfinger, 2024, https://doi.org/10.13140/RG.2.2.19463.00166, EV DVA Tool.

39. L. Wildersinn, D. Stottmeister, F. Jeschull, A. Groß, and A. Hofmann, "Decomposition of Binary Mixtures of DMC/EC, EMC/EC, and DEC/EC on Potassium Surfaces; GC, XPS, and Calculation," *ACS Applied Materials & Interfaces* 17, no. 6 (2025): 10055–10072, https://doi.org/10.1021/acsami.4c17461.

40. A. Hofmann, F. Müller, S. Schöner, and F. Jeschull, "Revealing the Formation of Dialkyl Dioxahexane Dioate Products from Ethylene Carbonate Based Electrolytes on Lithium and Potassium Surfaces," *Batteries & Supercaps* 6 (2023): e202300325, https://doi.org/10.1002/batt.202300325.

41. H. Onuma, K. Kubota, S. Muratsubaki, et al., "Phase Evolution of Electrochemically Potassium Intercalated Graphite," *Journal of Materials Chemistry A* 9, no. 18 (2021): 11187–11200, https://doi.org/10.1039/D0TA12607A.

42. B. Larhrib, L. Madec, L. Monconduit, and H. Martinez, "Optimized Electrode Formulation for Enhanced Performance of Graphite in K-Ion Batteries," *Electrochimica Acta* 425 (2022): 140747, https://doi.org/10.1016/j.electacta.2022.140747.

43. Z. Guo, K. Wang, Y. Zhao, et al., "Revisiting Potassium Intercalation in Graphite: An, *Operando* Characterisation and Computational Approach," *EES Batteries* 2 (2026): 163, https://doi.org/10.1039/D5EB00184F.

44. F. Jeschull, D. Brandell, K. Edström, and M. J. Lacey, "A Stable Graphite Negative Electrode for the Lithium–Sulfur Battery," *Chemical Communications* 51, no. 96 (2015): 17100–17103, https://doi.org/10.1039/C5CC06666B.

45. F. Jeschull, M. J. Lacey, and D. Brandell, "Functional Binders as Graphite Exfoliation Suppressants in Aggressive Electrolytes for Lithium-Ion Batteries," *Electrochimica Acta* 175 (2015): 141–150, https://doi.org/10.1016/j.electacta.2015.03.072.

46. H. Ota, Y. Sakata, A. Inoue, and S. Yamaguchi, "Analysis of Vinylene Carbonate Derived SEI Layers on Graphite Anode," *Journal of the Electrochemical Society* 151, no. 10 (2004): A1659, https://doi.org/10.1149/1.1785795.

47. Y. Surace, D. Leanza, M. Mirolo, et al., "Evidence for Stepwise Formation of Solid Electrolyte Interphase in a Li-Ion Battery," *Energy Storage Materials* 44 (2022): 156–167, https://doi.org/10.1016/j.ensm.2021.10.013.

48. S. Komaba, T. Itabashi, M. Watanabe, H. Groult, and N. Kumagai, "Electrochemistry of Graphite in Li and Na Salt Codissolving Electrolyte for Rechargeable Batteries," *Journal of the Electrochemical Society* 154, no. 4 (2007): A322, https://doi.org/10.1149/1.2472552.

49. A. L. Michan, B. S. Parimalam, M. Leskes, et al., "Fluoroethylene Carbonate and Vinylene Carbonate Reduction: Understanding Lithium-Ion Battery Electrolyte Additives and Solid Electrolyte Interphase Formation," *Chemistry of Materials* 28, no. 22 (2016): 8149–8159, https://doi.org/10.1021/acs.chemmater.6b02282.

50. R. Stockhausen, L. Gehrlein, T. Bergfeldt, et al., "Investigating the Reduction of Fluoroethylene Carbonate and Vinylene Carbonate in Lithium-Ion Cells with Silicon-Graphite Anodes," *Batteries & Supercaps* 8 (2025): e202400499, https://doi.org/10.1002/batt.202400499.

51. Q. T. N. Phan, J. Kawamura, and K. Kurihara, "Effect of Vinylene Carbonate on SEI Formation on $LiMn_2O_4$ in Carbonate-Based Electrolytes," *Physical Chemistry Chemical Physics* 24, no. 41 (2022): 25611–25619, https://doi.org/10.1039/D2CP02421G.

52. S. Oswald, M. V. Gorbunov, and D. Mikhailova, "Electron Spectroscopy Investigations of Potassium and Potassium-Intercalated Graphite with Battery Background," *Applied Surface Science* 655 (2024): 159614, https://doi.org/10.1016/j.apsusc.2024.159614.

53. L. Caracciolo, L. Madec, and H. Martinez, "XPS Analysis of K-Based Reference Compounds to Allow Reliable Studies of Solid Electrolyte Interphase in K-Ion Batteries," *ACS Applied Energy Materials* 4, no. 10 (2021): 11693–11699, https://doi.org/10.1021/acsaem.1c02400.

54. C. Xu, B. Sun, T. Gustafsson, K. Edström, D. Brandell, and M. Hahlin, "Interface Layer Formation in Solid Polymer Electrolyte Lithium Batteries: An XPS Study," *Journal of Materials Chemistry A* 2, no. 20 (2014): 7256–7264, https://doi.org/10.1039/C4TA00214H.

55. A. Smith, P. Stüble, L. Leuthner, A. Hofmann, F. Jeschull, L. Mereacre, "Potential and Limitations of Research Battery Cell Types for Electrochemical Data Acquisition," *Batteries & Supercaps* 6, no. 6 (2023): e202300080, https://doi.org/10.1002/batt.202300080.

56. A. W. Ells, R. May, and L. E. Marbella, "Potassium Fluoride and Carbonate Lead to Cell Failure in Potassium-Ion Batteries," *ACS Applied Materials & Interfaces* 13, no. 45 (2021): 53841–53849, https://doi.org/10.1021/acsami.1c15174.

57. Q. Liu, A. M. Rao, X. Han, and B. Lu, "Artificial SEI for Superhigh-Performance K-Graphite Anode," *Advanced Science* 8, no. 9 (2021): 2003639, https://doi.org/10.1002/advs.202003639.

58. P. A. Morozova, I. A. Trussov, D. P. Rupasov, V. A. Nikitina, A. M. Abakumov, and S. S. Fedotov, "Exploring the Role of Crystal Water in Potassium Manganese Hexacyanoferrate as a Cathode Material for Potassium-Ion Batteries," *Crystals* 11, no. 8 (2021): 895, https://doi.org/10.3390/cryst11080895.

59. T. Hosaka, T. Matsuyama, R. Tatara, Z. T. Gossage, and S. Komaba, "Impact of Electrolyte Decomposition Products on the Electrochemical Performance of 4 V Class K-Ion Batteries," *Chemical Science* 14, no. 33 (2023): 8860–8868, https://doi.org/10.1039/D3SC02111D.

60. L. A. Ma, A. J. Naylor, L. Nyholm, and R. Younesi, "Strategies for Mitigating Dissolution of Solid Electrolyte Interphases in Sodium-Ion Batteries," *Angewandte Chemie* 133, no. 9 (2021): 4905–4913, https://doi.org/10.1002/ange.202013803.

61. J. F. Schuster, L. A. Ma, C. A. O'Keefe, C. P. Grey, and R. Younesi, "Comparative Stability of the Solid Electrolyte Interphase in Potassium and Sodium Batteries," *Energy Advances* 5, no. 2 (2026): 146–150, https://doi.org/10.1039/D5YA00173K.

62. F. Holtstiege, A. Wilken, M. Winter, and T. Placke, "Running out of Lithium? A Route to Differentiate between Capacity Losses and Active Lithium Losses in Lithium-Ion Batteries," *Physical Chemistry Chemical Physics* 19, no. 38 (2017): 25905–25918, https://doi.org/10.1039/C7CP05405J.

63. F. Jeschull, Bat2dat: Analysis of Potentiostat Output for Battery Research, 2026, https://doi.org/10.5281/ZENODO.18643125.

Supporting Information

Additional supporting information can be found online in the Supporting Information section. Additional galvanostatic cycling data, dQ/dV plots of KVP/C and graphite half cells, GC-MS spectra, SEM micrographs of pristine KVP/C and graphite electrodes, XPS comparison with and without charge compensation, table listing of atomic percentages.